Multi-Resolution Level Sets with Shape Priors: A Validation Report for 2D Segmentation of Prostate Gland in T2W MR Images

Fares S. Al-Qunaieer · Hamid R. Tizhoosh ·
Shahryar Rahnamayan

Abstract The level set approach to segmentation of medical images has received considerable attention in recent years. Evolving an initial contour to converge to anatomical boundaries of an organ or tumor is a very appealing method, especially when it is based on a well-defined mathematical foundation. However, one drawback of such evolving method is its high computation time. It is desirable to design and implement algorithms that are not only accurate and robust but also fast in execution. Bresson et al. have proposed a variational model using both boundary and region information as well as shape priors. The latter can be a significant factor in medical image analysis. In this work, we combine the variational model of level set with a multi-resolution approach to accelerate the processing. The question is whether a multi-resolution context can make the segmentation faster without affecting the accuracy. As well, we investigate the question whether a premature convergence, which happens in a much shorter time, would reduce accuracy. We examine multiple semiautomated configurations to segment the prostate gland in T2W MR images. Comprehensive experimentation is conducted using a data set of a 100 patients (1,235 images) to verify the effectiveness of the multi-resolution level set with shape priors. The results show that the convergence speed can be increased by a factor of ≈ 2.5 without affecting the segmentation accuracy. Furthermore, a premature convergence approach drastically increases the segmentation speed by a factor of ≈ 17.9.

F. S. Al-Qunaieer · H. R. Tizhoosh (✉)
Systems Design Engineering, University of Waterloo,
200 University Ave. West, Waterloo, ON N2L 3G1, Canada
e-mail: tizhoosh@uwaterloo.ca

S. Rahnamayan
Electrical and Computer Engineering, University of Ontario Institute
of Technology (UOIT), 2000 Simcoe Street North, Oshawa,
ON L1H 7K4, Canada

Introduction

The use of level set methods has been increasing in recent years since they do not, in contrast to active contours such as snakes, rely on contour parametrization. This feature enables level set segmentation to adjust better to topological changes. As well, level set algorithms can be easily extended to higher dimensions. In addition, they are mathematically well-established, making them better to understand, analyze, and implement. Furthermore, level sets are defined implicitly, so, topological changes of the curve, such as splitting and merging, and corner and cusp development are handled much easier than other active contour methods, such as the explicit snakes technique [1]. However, the level-set methods propagate a curve using a higher dimensional function and their numerical solutions need small time steps to achieve stable curve evolution [2], such that the computation time can drastically increase. Hence, designing fast level set algorithms is the goal of many recent research works including this paper.

To verify the performance of level set segmentation and in order to assess the performance of any modification, one needs a real-world case. Prostate imaging is needed for several purposes, such as cancer detection and prostate volume estimation for diagnosis, active surveillance, biopsy, and treatment planning. For radiation therapy, for instance, generally CT images are employed whereas in some cases, registering MR images, in order to exploit their information via fusion with CT scans, may also be useful. Prostate imaging using MRI provides high soft-tissue contrast and distinction of anatomic structures. This advantage can be exploited if we register MR images to CT or ultrasound scans to fuse

information from two different modalities. The manual prostate segmentation in MR images is a time-consuming task. Thus, proposing automated or semi-automated methods to segment the prostate gland in MR images is desirable.

In this paper, a semiautomated multi-resolution level set algorithm is used for 2D segmentation of prostate gland in T2W MR images. A multi-resolution approach is used to accelerate the convergence speed. A shape-prior method is utilized to compensate for the weak edges and similar tissue structures surrounding the prostate. Comprehensive experimentation is conducted using a large data set of MRI prostate images (image data of 100 patients consisting of 1,235 images to be segmented) to verify the effectiveness of the used method.

The paper is organized as follows: in "Prostate Segmentation", other works on prostate segmentation are briefly reviewed. "Level Set for Image Segmentation" provides a background review on level set methods, using prior shapes and existing approaches to employ multi-resolutions. In "Multi-Resolution Level Set for Prostate Segmentation in MR Images", the proposed combination of level set with shape priors and multi-resolution is laid out. "Experimental Settings" describes the experimental settings including the dataset, construction of the shape priors, performance measures, and implementation environment. "Results" presents and discusses the results including, accuracy and time evaluations, the effect of ROI variability, leave-one-patient-out evaluation, and the results of a premature convergence. "Discussion and Concluding Remarks" are presented in the last section.

Prostate Segmentation

Because of the recent attention to prostate MR imaging, there is only a few research works, e.g., compared to transrectal ultrasound imaging, related to their segmentation. Statistical shape models have been used for this purpose. For instance, an active shape model (ASM) approach is proposed for prostate segmentation [3]. In other paper, region-based statistical appearance model (SAM) from texture features is constructed and integrated with level set based statistical shape model (SSM) for 3D MRI prostate segmentation [4].

Several works utilize active contours for prostate segmentation in MR images. Tsai et al. use a region-based level set with shape prior to 3D segmentation of prostate MRI [5]. Snakes and region-growing are utilized in another work for prostate, bladder, and rectum segmentation [6]. Zhang et al. propose an interactive method utilizing edge-based level set [7]. Liu at el. compute deformable elliptical model and use it to initialize region-based level set with shape prior [8].

Other researchers use probabilistic approaches. Farjani et al. introduced a 3D segmentation technique based on the maximum a posteriori (MAP) estimate of a log-likelihood function consisting of three descriptors: intensity, shape prior, and spatial interaction [9, 10]. The authors experimentally compare their results in [9] with [5] and have achieved significantly better performance in terms of accuracy. Makni et al. introduced Bayesian a-posteriori segmentation based on Markov field [11]. A statistical shape model was used as a priori knowledge.

Various other methodologies are used for prostate segmentation in MR images. For instance, semiautomatic approaches based on atlas registration have been proposed [12, 13]. Firjany et al. segment the prostate gland by using graph cuts to optimize an energy function constructed from intensity level, shape information, and spatial information [14]. A method using wavelet multi-scale products (MWP) has been proposed as well [15, 16]. The border of prostate is found by adaptively tracing the magnitude of WMP near the prostate gland. Samiee et al. propose a semiautomatic approach for prostate segmentation by computing edge direction in the region around prostate [17]. By transforming prostate image into polar space, Zwiggelaar et al. segment the prostate by line detection and non-maximum suppression [18]. Sahba et al. [19, 20] use locally adaptive enhancement [21] and Kalman filter to segment the prostate gland. Rahnamyan et al. [22] focus on automated initialization of snakes, whereas Bustince et al. [23] use ignorance functions for prostate thresholding.

Prostate MR imaging provides high sensitivity and contrast supporting a better visual inspection by clinicians. Segmentation of MR images, however, can be more difficult due to their richness and the presence of many edges. We use prostate MR images, both with and without endo-rectal coils, to verify the hypothesis whether combining a multi-resolution scheme with level set segmentation can deliver accurate and fast results.

Level Set for Image Segmentation

Level sets were introduced in 1988 for interface propagation [1]. They have been used in many applications such as computational fluid mechanics [24], computer graphics [25], shape optimization [26], inverse problems [27], and image processing [2]. The contour is defined implicitly by using a Lipschitz-continuous function $\phi(x,y)$, called level set function. Usually, the contour is defined at the zero th level of $\phi(x,y)$ such that positive and negative values represent different regions. The evolution of the curve is performed implicitly as the level set function evolves. Since the contour is defined implicitly with a function of higher dimension, topology changes are handled automatically. The most common

method for defining initial level set function $\phi_0(x,y)$ is using the sign distance function of the initial contour.

Geometric active contours were introduced as the first implementation of level set formulation of active contours to solve an image segmentation problem [28]. A similar method was proposed by Malladi et al. [29, 2]. Geodesic active contours were proposed by Caselles et al. [30], [31]. The authors define a geodesic curve as "a local minimal distance path between given points". The objective is to find geodesic (minimum distance) curves in a Riemanian space with metric derived from the image content. Similar active contour models have been proposed in other works [32], [33]. In addition to curve length minimization, other papers propose area minimizing term to the speed function [34]. Because edge-based level set methods rely on local features (the gradient of the image), noise can greatly affect the performance of the algorithm.

Region-based active contour algorithms exploit the characteristics of regions, such as intensity distribution or texture, for curve evolution. One of the early and well-known methods is proposed by Chan and Vese. The authors proposed a level set method to minimize Mumford-Shah segmentation model [35] for piecewise constant approximation of the image [36]. A piecewise smooth approximation version has been introduced as well [37]. In this method, smoothed partial images represent each partition. Similar active contour models and formulations have been proposed in other reports [38, 39].

Shape Priors

Although the level set approach is considered a good segmentation method, many shapes remain difficult to segment. This could be due to noise, objects' occlusion, or low contrast among background and objects. Adding a constraint to search for certain shapes was considered by several researchers, and has obtained good results in some applications.

Chen et al. proposed a method that incorporates the shape prior into the level set formulation [40]. For n images with the curves $C_1,...,C_n$ representing the segmented objects in the images with different sizes and orientations, the shape prior, C^*, is defined by calculating the average shape of the n curves. The suggested level set formulation is given by

$$\min_{\phi,\mu,R,T} \int_\Omega \delta(\phi)\left\{g(|\nabla I|) + \frac{\lambda}{2}d^2(C^*, \mu RC + T)\right\}|\nabla\phi|, \quad (1)$$

where C is the contour represented by the zero th level of the level set function ϕ, μ is scale transformation matrix, R is the rotation transformation matrix, λ is a weight, $g(\cdot)$ is an edge detection function, δ is the Dirac function, and T is a translation transformation vector. The function d is defined as the distance between the point (x,y) on $(\mu RC+T)$ and the shape prior C^*.

Tsai et al. proposed a method for capturing the shape prior by utilizing principal component analysis [5]. The authors represented the shape as the zero level curve imposed on the level set $\phi(w)$, which is defined by the mean shape $\overline{\phi}$ and the weighted m eigenshapes $\{\phi_1,...,\phi_m\}$, defined from the training data as in

$$\phi(w) = \overline{\phi} + \sum_{i=1}^m w_i\phi_i, \quad (2)$$

where w_i are the weights for eigenshapes.

Leventon et al. used a similar method to extract the shape prior using principal component analysis [41]. In addition, the maximum a posteriori (MAP) position and shape of the object is estimated at each step of the surface deformation based on the prior shape and image properties. The authors extended geodesic active contours by adding the shape information.

Inspired from two-view geometry, Riklin-Raviv et al. proposed an extension to Chan and Vese method by including shape prior [42]. The authors used two images, one as a reference and the other one as target image. The object in the reference image is used to construct the prior shape $\widehat{\phi}$ by using planar projective homography. The dissimilarity between the zero level set ϕ and the zero level set $\widehat{\phi}$ is used to derive the energy function that evolves the level set ϕ. Other work embedded the knowledge of the symmetry of objects into level set function formulation [43].

Bresson et al. proposed a level set function that incorporates edge, region, and shape terms [44]. We use this method as our base/parent algorithm to verify the effect of both shape prior and multi-resolution. We describe this approach in more details in "Multi-Resolution Level Set for Prostate Segmentation in MR Images".

Multi-Resolution Level Set

Multi-resolution image analysis concerns representation and processing of images in different resolutions. While some features cannot be detected at one resolution, they may be detected at others. As well, the effect of noise and false edges may be reduced at lower resolutions. These are the main motivations of multi-resolution analysis. Several multi-resolution techniques have been proposed in literature to improve level sets.

Pyramid multi-resolution analysis is a well-known technique in image processing. Images of different resolutions are created by filtering and subsampling the original image. Gaussian pyramid has been utilized to enhance edge-based level set active contours [45]. The curve initialization is performed on the coarsest resolution and propagation proceeds

with finer resolutions. Similar methodology has been employed to segment ultrasound echocardiographic images [46, 47].

Scale-space representation has been used for multi-resolution analysis of images as well [48]. Set of images are created with different smoothness scales. As scale of smoothness is increased, the fine-scale structures in the image are suppressed. Bresson et al. proposed a level set formulation of active contours in scale-space [49]. The evolution equation of the suggested framework is based on the Polyakov functional. Several applications along multi-scale segmentation have been proposed.

As a well-known multi-resolution analysis tool, wavelet transform has been employed to enhance active contours in several research projects. Curvelet, which is a multi-scale and multi-directional geometric wavelet transform, has been used to enhance geodesic active contours [50]. An edge map is obtained using curvelet thresholding. Initialization is performed in the coarsest resolution, and for each subsequent finer resolution, the level set function ϕ is defined as the converged level set function of the previous resolution. Al-Qunaieer et al. proposed a method to accelerate region-based level set image segmentation [51]. The authors used wavelets to decompose the image into three resolutions, and start the curve evolution from the coarsest resolution. The achieved results confirmed that using multi-resolution reduces the effect of noise for large objects and accelerates the convergence rate of the segmentation algorithm.

Multi-Resolution Level Set for Prostate Segmentation in MR Images

In this paper, we extend level set image segmentation with shape-prior method (according to [44]) to take advantage of a multi-resolution approach. This method was selected because its formulation incorporates three terms: the shape term (accounts for object's shape), the region term to attract the shape-prior globally toward homogeneous intensity regions, and the local edge term to attract the curve toward local variations near the object. A shape prior is constructed by applying principal component analysis (PCA) on the signed distance functions of the zero th level set of training contours. Only the few first principal modes are needed to capture the largest variations in the training set while redundancy is removed. The shape prior is constructed as

$$\widehat{\phi} = \overline{\phi} + W_p x_{pca}, \tag{3}$$

where $\overline{\phi}$ is the mean shape, W_p contains the first p principal components, and x_{pca} is the vector of eigencoefficients.

Using a multi-resolution approach reduces the noise in the coarse scales. Also, at the coarsest level, weak edges are ignored and the contour will be only attracted to the strong edges. In addition, regions become more homogeneous as the resolution is reduced. If the initialization of the curve begins with a coarse version of the image, the convergence will be fast because many details are omitted and only the main features and edges remain. This enables us to implement a faster algorithm. Few multi-resolution approaches have been reported in literature as discussed in the previous section, but none of them has tried to segment the prostate gland in MR images. In this paper, we analyze the performance of the proposed multi-resolution extension in terms of accuracy and running time in more details.

Algorithm 1 describes how shape priors are created during a training phase. T is the training set, which consists of manually segmented images. The curves defining the segmented prostate are extracted from the training set and stored in C. The signed distance function (SDF) is calculated for each curve for the shape-prior construction. Then, all signed distance curves in C are aligned (see [52]). After that, the average shape, $\overline{\phi}$, is calculated from C and the first p principal components are computed and stored in W_p.

The pseudo-code of the proposed approach is presented in Algorithm 2. The shape priors S are extracted from the training set as defined in Eq. (3). r is the number of levels of resolution and ROI is the region of interest (a rectangle around the prostate gland). The preprocessing stage consists of noise removal and contrast enhancement ("Preprocessing"). The image I and shape-prior S are decomposed into r levels of resolutions using Gaussian pyramid. Each lower resolution level is obtained by using a 5×5 low-pass filter on the previous level. For levels $0 < l < r$ and image I of size $N \times M$, the pyramid defined as [53]

$$I_l(i,j) = \sum_{m=-2}^{2} \sum_{n=-2}^{2} w(m,n) I_{l-1}(2i+m, 2j+n), \tag{4}$$

where $i=1,\ldots N, j=1,\ldots M$, and $w(\cdot)$ is a Gaussian-like kernel. The result of image decomposition is stored in I_k, where $k=0,\ldots,r$ and r is the lowest resolution, thus I_0 is the original image and I_r is the coarsest resolution. Similarly, the shape prior S is decomposed and stored in S_k, where $k=0,\ldots,r$. Starting from the coarsest image resolution I_r, Bresson algorithm is run on I_r using S_r for shape-prior. The curve is initialized with an ROI (the rectangle around the prostate is used as the initial curve). As the current resolution is not the resolution of the original image, the converged curve of the current resolution is up-sampled for each next (finer) resolution. For

each resolution i, the shape prior S_i is used to guide the evolution of the level set function on image I_i. The

algorithm continues until the curve converges in the original resolution.

Algorithm 1: Shape-Prior Training

$T = [t_1, t_2 \dots, t_n]$ /* training set */
for $i = 1$ to n **do**
    $C_i =$ ExtractCurve(T_i) /* extract contours */
    $C_i =$ SDF(C_i); /* signed distance function */
end for
Align(C), $C = [c_1, c_2 \dots, c_n]$ /* align contours */
$\bar{\phi} =$ MeanShape(C) /* generate average shape */
$W_p =$ PCA(C) /* find principal components */

Algorithm 2: Multi-resolution approach

I = input image
S = shape-prior, see Eq. (3) and Algorithm 2
r = number of resolutions
ROI = region of interest
Pre-Processing
I = NoiseRemoval(I)
I = ContrastEnhancement(I)
Multi-Resolution Decomposition (Pyramid)
$I_k =$ Pyramid $_r(I)$, $k = 0, \dots, r$
$S_k =$ Pyramid $_r(S)$, $k = 0, \dots, r$ /* r is the lowest resolution */
Multi-Resolution Propagation
for $i = r$ to 0 **do**
    Shape-prior = S_i
    if $i = r$ **then**
        Initialize curve, on I_r within ROI
    else
        initial curve $\leftarrow$ up-sampled curve
    end if
    Run Bresson algorithm on I_i using S_i
    if $i > 0$ **then**
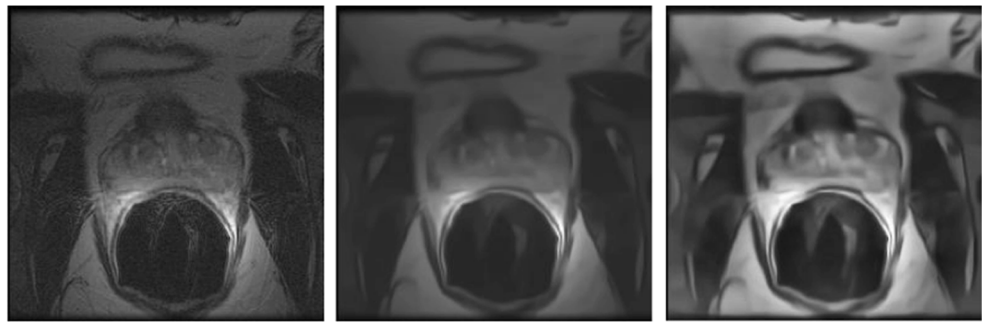   Up-sample curve to the $(i-1)^{th}$ resolution
    end if
end for

Preprocessing

Prostate MR images are generally difficult to segment, this is, among others, due to the low contrast among prostate and adjacent tissues, the fuzzy boundaries of prostate, and many

other edges in vicinity of the prostate border (e.g., rectum edges). In order to segment the prostate accurately, preprocessing steps are required for any method. Two preprocessing steps were applied to each image before curve propagation started. The first step is for noise elimination. For this purpose,

Fig. 1 Preprocessing steps (from *left* to *right*): input image, after noise removal, and after contrast enhancement

a non-local adaptive non-parametric filtering approach, proposed by Dabov et al. [54] was utilized. Then, a contrast enhancement using contrast-limited adaptive histogram equalization was applied [55]. Figure 1 illustrates the output image of both noise removal and contrast enhancement steps. These steps were the same for all tested methods. Please note that the time spent on preprocessing has not been included in the time measurements to evaluate the performance of the proposed approach.

Experimental Settings

In this section, the experimental settings will be described. We use a large dataset consisting of image data of 100 patients (1,235 images) to verify whether embedding level sets in a multi-resolution framework can expedite the segmentation process while maintaining the same achievable accuracy level. We will refer to the level set method according to Bresson et al. [44] as LS_B and the proposed multi-resolution extension as LS_B^{MR}.

Dataset

Prostate MR images used in this paper have been collected from the online archive database "Prostate MR Image Database" [56]. The database contains MR volume data of more than 100 patients and is provided by Brigham and Women's Hospital, the National Center for Image-Guided Therapy and Harvard Medical School. Different machines were used to obtain the images. All images are T2 weighted with or without endo-rectal coil but they have been with different MR machines and exhibit different qualities. The slice thickness ranges from 2 to 4 mm. The field of view is ranging from 90 to 140 %. The dataset has been downloaded and converted to DICOM images. An oncologist has manually segmented the prostate gland in all images. We refer to these manually segmented images as gold standard images for the algorithms. Such images are used to construct the shape priors and to verify the accuracy of the tested algorithms. The number of images for each patient is different. Some patients

have more than one set of images (multiple sets captured with different configurations). Some of the images are 256×256 pixels, while others are 512×512 pixels.

Constructing the Shape Priors

In order to construct the shape priors, 30 % of the patients were used for training, while the remaining datasets are used for testing. To test the effect of shape priors on the segmentation results, a "leave-one-patient-out" evaluation was also conducted using 10 randomly selected patients. Curves describing the segmented prostate glands are extracted from the gold standard images, and then aligned with each other. PCA is applied on the aligned signed distance function of the training curves in order to select the first p principal components that have 98 % fitting with the training curves. The Eq. (3) is used for the shape-prior construction.

Prostate images may be divided into three distinctive regions with respect to shape diversity/irregularity: the top slice(s) (apex), the bottom slice(s) (base) and slices in between (midgland). Because of this distinction, three different shape priors are constructed. The used shape priors are illustrated in Fig. 2. Needless to say that for the prostate gland segmentation in this approach, the internal zones (central and peripheral zones) do not play any role as we are looking to extract the gland boundaries.
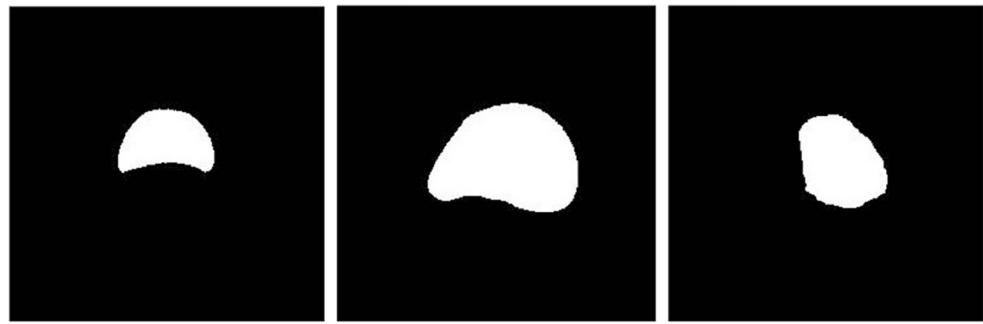
Performance Measures

The numerical results of LS_B^{MR} and LS_B are compared in terms of execution time and accuracy for each level of resolution. Time is measured for the complete execution of the two algorithms including initialization phase for both, and image and shape decomposition in LS_B^{MR}.

Two measures are used to calculate accuracy, namely dice coefficient D and Hausdorff distance d_H. The dice coefficient is calculated by [57]

$$D = \frac{2\left|I_n \bigcap I_G\right|}{\left|I_n\right| + \left|I_G\right|}, \tag{5}$$

Fig. 2 From *left* to *right*: shape priors for apex, midgland, and base

where I_n is the segmented image, I_G is the gold standard image, and $|\cdot|$ is the set cardinality. The Hausdorff distance is calculated by [58]

$$d_H = \max(h(I_n, I_G), h(I_G, I_n)), \tag{6}$$

where

$$h(I_n, I_G) = \max_{a \in I_n} \min_{b \in I_G} \|a-b\|. \tag{7}$$

Since we are using a large dataset, the mean, standard deviation, and the 95 % confidence interval of all measurements are calculated.

Implementation Environment

The experiments were conducted using a PC with a CPU speed of 2.20 GHz and 8 GB of RAM. The operating system was Windows 7 (64-bit version). The program was written and run with 64-bit version of Matlab. All software packages have been accessed under research licensing at the University of Waterloo.

Results

LS_B^{MR} is a semi-automatic approach such that the region of interest (ROI) is assumed to be provided by the user. This is a rectangle around the prostate gland that limits the segmentation to a smaller portion of the image. In our tests, the ROI of an input image is a rectangle (bounding box) that touches the edges of the shape in the corresponding gold standard image,

Table 1 Parameters setting

Parameter	Value
Num. of iterations for re-initialization	5
Time steps	1
Spatial transformation	Affine
Weight for the boundary term	1
Weight for the shape term	1/3
Weight for the region term	10

but enlarged by 15 % of its width in each direction. The number of resolution levels is empirically chosen to be three ($r=3$). It s worth to mention that the choice of the number of resolutions could greatly affect the performance of LS_B^{MR}. The evolution of the curve for both algorithms is stopped if there is a change less than $\varepsilon=15$ in five consecutive iterations, or if the number of iterations exceeds 1,000. Parameters for both algorithms were empirically set to same values (Table 1). To be consistent, all images are assumed to be of size 256×256. If a 512×512 image is encountered, it is resized.

In this section, multiple experiments are conducted:

1. Evaluate the performance of LS_B^{MR} and compare it to LS_B
2. Analyze the sensitivity of the algorithm to manual ROI selection
3. Verify the effect of the shape priors on the performance of LS_B^{MR} via a leave-one-patient-out
4. Investigate the effect of premature convergence

Accuracy and Speed Evaluation

In this experiment, the shape priors are constructed using 30 % of the available data (the images of one patient are either in training or in testing set). The first p principal components that have 98 % fitting with the training curves are selected. The number of principal components fitting this criteria are 5 for apex, 4 for base, and 4 for midgland. Noise removal and contrast enhancement are applied to all images. The first two slices were segmented using the shape prior for apex, the last two using the shape prior for base, and the remaining in between using the shape prior for midgland. It is worth mentioning that a small distance between the slices naturally generates many images, hence, leading to several slices representing each apex, base, and mid-gland sections. However, since we use the shape prior for initialization, this will not affect the processing as for a fine slice thickness/gap, e.g., smaller than 1 mm, adjacent slices will be very similar. The rectangle representing the ROI was used as curve initialization. Both methods were run for all images, and the performance measures (dice value, Hausdorff distance, and time) along with the segmented image were recorded. Selected

Table 2 Sample results for some individual images

Image# (part)	LS_B			LS_B^{MR}			Speed-up
	D (%)	d_H	Time (s)	D (%)	d_H	Time (s)	
Apex	88	3.46[a]	63	86[a]	3.74	29[a]	2.1
Apex	82[a]	4.00[a]	66	81	4.12	46[a]	1.4
Midgland	91	4.47[a]	148	93[a]	5.29	58[a]	2.5
Midgland	85	4.00[a]	84	86[a]	4.24	32[a]	2.6
Midgland	91[a]	5.66[a]	93	89	5.74	44[a]	2.1
Midgland	91[a]	4.69[a]	181	90	5.00	70[a]	2.6
Base	93[a]	3.61	81	90	3.46[a]	49[a]	1.6
Base	92[a]	4.12[a]	68	90	4.58	30[a]	2.3
Midgland	58	5.92[a]	36	59[a]	5.92[a]	27[a]	1.3
Midgland	63	5.00	29	67[a]	4.90[a]	18[a]	1.6
μ	83	4.49	85	83	4.70	40	2.1
σ	12	0.78	45 0	11	0.78	15	

[a] Better results

sample results are presented in Table 2. Both algorithms converged before reaching maximum number of iterations (i.e., 1,000) for all images.

Analysis of Table 2 As it can be seen, the accuracy remains the same (around 83 % for both methods), whereas the computational time decreases from 85±45 s (for LS_B) to 40±15 s (for LS_B^{MR}). This represents an speed-up factor of ≈2.1.

Because of the large number of images (1,235 segmented slices), the results are summarized per patient. The dice value D and Hausdorff distance d_H along with time averages and standard deviations are calculated for all patients. The overall performance of the algorithms is summarized in Table 3. Figure 3 shows sample segmentations.

Table 3 Overall summary of results (95 % confidence interval) for both methods

Region	Metric		
Apex	D	[61 %, 69 %]	[66 %, 70 %][a]
	d_H	[5.76, 6.28]	[5.75, 6.17][a]
	Time (s)	[129, 170]	[55, 67][a]
Midgland	D	[76 %, 79 %]	[77 %, 80 %][a]
	d_H	[5.50, 5.85][a]	[5.53, 5.87]
	Time (s)	[105, 128]	[43, 49][a]
Base	D	[80 %, 83 %][a]	[72 %, 76 %]
	d_H	[4.77, 5.26][a]	[5.10, .64]
	Time (s)	[87, 107]	[34, 39][a]
Overall	D	[76 %, 79 %]	[77 %, 80 %][a]
	d_H	[5.50, 5.85][a]	[5.53, 5.87]
	Time (s)	[105, 128]	[43, 49][a]

[a] Better results

Analysis of Table 3 The overall performance of the two algorithms are extremely similar in terms of accuracy. However, the obvious difference is in the running time, where LS_B^{MR} is on average 2.5 times faster than LS_B. It is an intuitive expectation that processing in lower resolutions should be much faster than higher ones. Furthermore, the initialized curves in the original resolution in LS_B^{MR} are closer to the prostate boundaries than in LS_B. This results in a lower number of iterations in the original resolution, hence shorter time. The segmentation of midgland slices is generally easier than apex/base since, depending of slice thickness, the first and last few slices may exhibit higher shape irregularities. It can be observed from Table 3 that midgland segmentation is more accurate than apex/base for LS_B^{MR}, which is expected, because the midgland is anatomically more consistent/regular than apex and base. However, base segmentation for LS_B is more accurate than midgland. A paired t test (with 95 % confidence interval) between methods was performed as well. The null-hypothesis testing for both dice and Hausdorff measures were not rejected, while the null-hypothesis was rejected for the time. One can conclude that the speed improvement was statistically significant, while the accuracies can be assumed to be the same. Sample curve propagation is illustrated in Fig. 4, where the first three rows are the resolutions from lowest to highest of LS_B^{MR} and the last row is the propagation in LS_B. It can be observed that for any finer resolution, the curve initialization is much closer to the prostate. This explains the fewer number of iterations in the original resolution, and thus faster convergence. Outputs of each resolution are shown in Fig. 5.

Effect of ROI Variability

As mentioned before, the proposed method is semi-automated and requires input (drawing an ROI) from an experienced user. Since we needed to automate the testing for the large number of
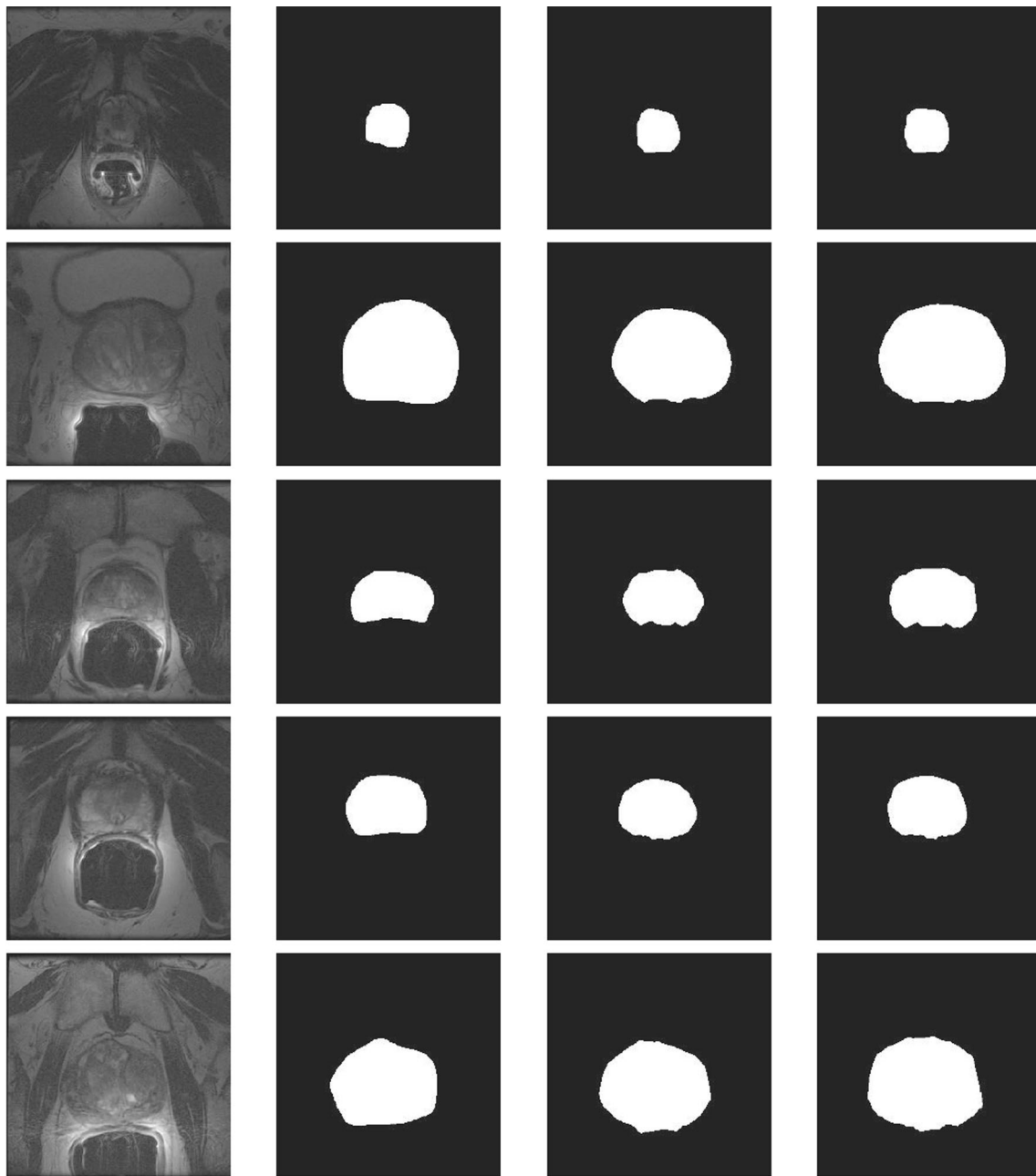
Fig. 3 Sample output segmentation (from left to right): input image, gold standard segment, Bresson, MR-Bresson

images, the ROI was extracted from the gold standard images (bounding box around the segment enlarged by 15 % of its width on all sides). The input ROI of the user (clinicians/doctors) will not be consistent with respect to its size. As well, a user-drawn ROI may not always be centered around the prostate gland; it is prone to variability in location and size. Thus, eight random patients were selected to be tested using two new settings of ROI. The first is with larger size (25 % of the bounding boxes' width), and another with random length/width variations such that it may not be centered around the prostate.

The results of using larger ROI are presented in Table 4.

Analysis of Table 4 Because the initial curve was larger (farther away from the prostate boundaries) than the previous experiment, the dice values are decreased. On the other hand, the Hausdorff distance and the processing times are increased. While dice value is decreased, compared with the previous experiment, for the multi-resolution level set, it decreased more for the level set because the curve can be attracted to the desired local features in the lower resolutions. For the same reason, the processing of the multi-resolution approach time did not change much compared to LS_B.

For the next experiment, the ROI was constructed by increasing each side of the ROI by $w \cdot r$, where w is 25 % of
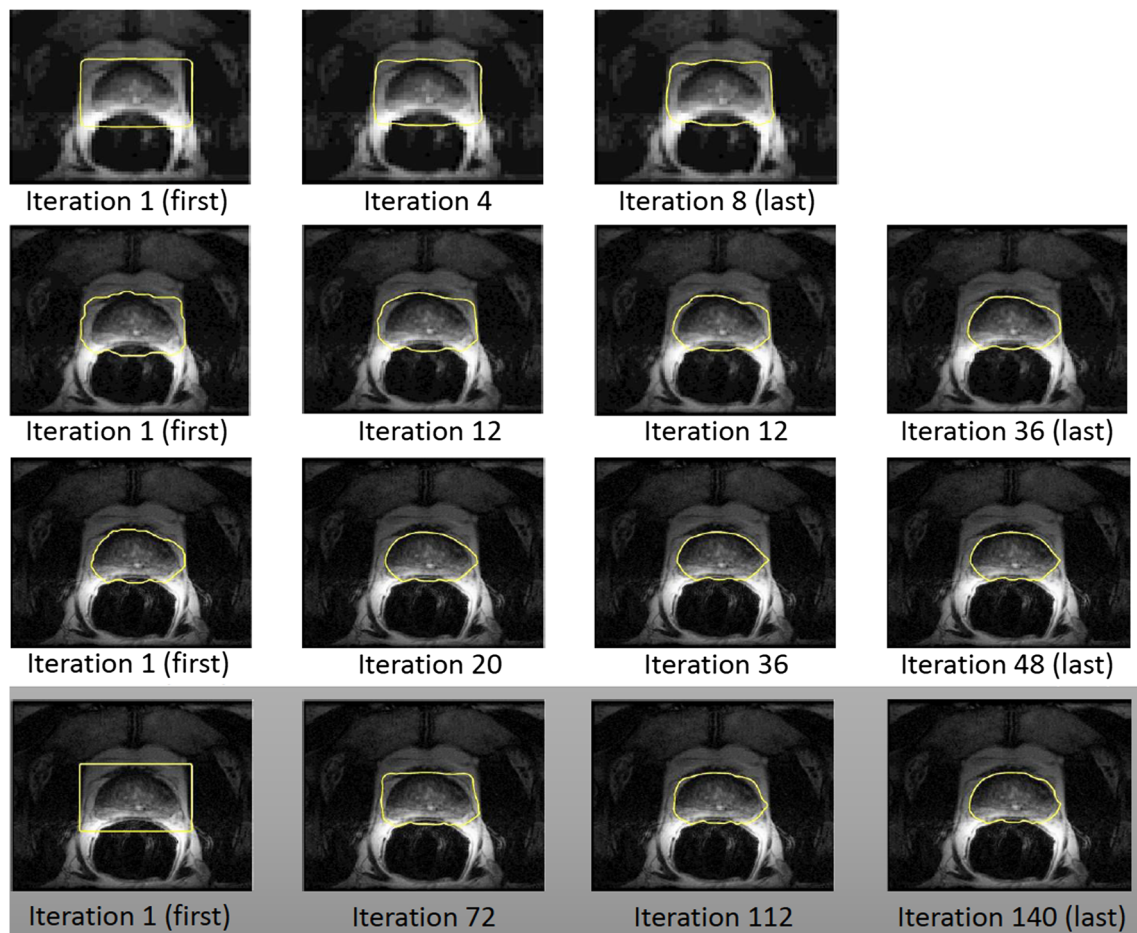
Fig. 4 Curve propagation for LS_B^{MR} and LS_B (brightness adjusted to facilitate visual inspection). The *first three rows* are for the three resolutions of LS_B^{MR}, starting from the coarsest. The *last row* is for LS_B (for clarity the images are scaled to be of the same size)

corresponding side and r is a uniformly distributed random number between zero and one. The results of using this ROI are presented in Table 5.

Analysis of Table 5 The results of using random ROI are closely comparable with the previous experiment. The dice values are the same for LS_B, Hausdorff distance is slightly increased, while time is decreased. For LS_B^{MR}, the dice values are slightly better, while Hausdorff distance and time are slightly decreased. These results suggest that randomness in ROI position can minimally affect the performance of both methods.

The change in accuracy and time in these two experiments indicate that curve initialization can affect the performance of the curve propagation and convergence. While the size of ROI can noticeably affect the performance of the algorithms, a slight shift in location of the ROI can minimally change the results.

Leave-One-Patient-Out Evaluation

In the previous subsections, the used shape priors were constructed from 30 % of the dataset. To assess the effect of the shape priors variation, a leave-one-patient-out evaluation on

Fig. 5 Resolution levels (for clarity, the images are scaled to be of the same size)

Table 4 The effect of larger ROIs

Patient#	LS_B			LS_B^{MR}		
	D	d_H	Time (s)	D	d_H	Time (s)
	77 %±8 %	5.49±0.41	163±59	80 %±4 %[a]	5.43±0.81[a]	70±31[a]
	70 %±26 %	6.16±1.9	216±61	79 %±2 %[a]	5.8±0.64[a]	81±56[a]
	75 %±11 %	6.91±0.98	206±71	79 %±4 %[a]	6.39±1.1[a]	72±25[a]
	69 %±20 %	5.32±1.03	125±75	80 %±5 %[a]	4.46±0.62[a]	39±8[a]
	64 %±21 %	5.94±1.26[a]	114±81	65 %±24 %[a]	6.36±1.82	77±121[a]
	82 %±5 %[a]	5.36±0.7[a]	206±33	77 %±21 %	5.46±1.18	104±113[a]
	73 %±10 %[a]	6.86±1.5	151±64	73 %±16 %	6.61±1.57[a]	49±582[a]
	77 %±18 %	5.58±1.6	119±57	79 %±3 %[a]	4.89±0.7[a]	38±10[a]
Larger ROI	73 %±15 %	5.95±1.17	163±63	77 %±10 %[a]	5.68±1.06 %[a]	66±53[a]
Fixed ROI	78 %±13 %	5.52±1.21	124±37	80 %±9 %[a]	5.51±0.79 %[a]	44±13[a]

[a] Better results

10 randomly selected patients was performed. The results are presented in Table 6.

Analysis of Table 6 It can be seen that the overall performance is slightly better in terms of both accuracy and time, though the improvement in time is much better for LS_B method. These results show that shape priors can noticeably affect the convergence time of the used method, and slightly affect the accuracy.

LS_B^{MR} Premature Convergence

As discussed in "Accuracy and Speed Evaluation", convergence in original image resolution is much slower than coarser resolutions. Thus, reducing the number of iterations in this resolution is the primary goal to achieve faster convergence. This was achieved in previous experiments by propagating up-sampled converged contours in lower resolutions to higher ones. However, the resolution zero (the original image) may still require multiple iterations for the contour to converge. The question arises whether it is really necessary to climb the resolution pyramid up to the original level, or one could simply stop at a lower resolution and deliver the up-sampled contour as final result. To answer this question, the experiment in "Accuracy and Speed Evaluation", was repeated for LS_B^{MR}, but this time stopping at resolution 1. The resulting curve is then up-sampled to original resolution and considered as the final segmentation. The shape priors are the ones used in "Accuracy and Speed Evaluation". The overall performance is summarized Table 7.

Analysis of Table 7 It can be observed that the speed is considerably increased by a factor of 7.6 for LS_B^{MR} and 17.9 for LS_B. The accuracy is slightly enhanced too. A paired t test between premature version of LS_B^{MR}, LS_B^{MRP}, was performed with a confidence interval of 95 % for dice, Hausdorff, and time. The null hypothesis for both Hausdorff distance and time was rejected.

Discussion and Concluding Remarks

In this paper, we have used multi-resolution level set method with shape priors for prostate segmentation in T2 weighted magnetic resonance (MR) images.

Table 5 The effect of ROI variability

Patient#	LS_B			LS_B^{MR}		
	D	d_H	Time (s)	D	d_H	Time (s)
	78 %±6 %[a]	5.78±0.78	111±38	78 %±7 %	5.64±1.09[a]	48±17[a]
	81 %±8 %	6.64±0.94	144±66	82 %±9 %[a]	6.36±0.65[a]	49±18[a]
	78 %±9 %	7.15±0.86	150±62	82 %±7 %[a]	7.01±0.92[a]	58±17[a]
	76 %±9 %	5.72±0.8	65±27	83 %±5 %[a]	5.25±0.89[a]	34±10[a]
	70 %±11 %	6.12±0.62	56±26	77 %±4 %[a]	5.77±0.55[a]	32±8[a]
	81 %±11 %	5.43±0.67	151±26	84 %±8 %[a]	5.22±0.69[a]	58±12[a]
	81 %±8 %	6.36±1.48	166±47	82 %±8 %[a]	6.33±1.4[a]	57±19[a]
	76 %±9 %[a]	5.98±1.02	88±45	76 %±10 %	5.81±0.68[a]	36±9[a]
Random ROI	78 %±9 %	6.15±0.9	116±42	81 %±7 %[a]	5.92±0.86[a]	46±14[a]
Fixed ROI	78 %±13 %	5.52±1.21	123±37	80 %±9 %[a]	5.51±0.79 %[a]	44±12[a]

[a] Better results

Table 6 Leave-one-patient-out evaluation (LOPO) for 10 randomly selected patients (better results highlighted in gray shading)

Patient#	LS_B			LS_B^{MR}		
	D	d_H	Time (s)	D	d_H	Time (s)
	77 %±4 %	4.93±0.36[a]	69±10	80 %±5 %[a]	4.96±0.7	29±6[a]
	77 %±4 %	5.63±0.53	110±32	80 %±4 %[a]	5.63±0.52[a]	49±22[a]
	87 %±3 %[a]	5.98±0.81[a]	160±19	85 %±8 %	6.42±0.9	47±15[a]
	58 %±21 %	6.44±2.8	55±14	63 %±13 %[a]	5.2±0.55[a]	28±6[a]
	66 %±7 %	4.91±0.52[a]	59±14	70 %±8 %[a]	5.31±0.48	31±7[a]
	79 %±3 %	6.19±0.43[a]	95±8	81 %±2 %[a]	6.38±0.58	34±6[a]
	87 %±3 %[a]	5.77±1.16[a]	194±42	86 %±2 %	5.89±1.27	68±18[a]
	79 %±4 %	5.82±1.2[a]	103±21	80 %±7 %[a]	5.96±1.28	36±6[a]
	82 %±6 %[a]	5.99±0.67[a]	160±23	79 %±9 %	6.22±0.71	56±15[a]
	83 %±5 %[a]	5.98±0.73[a]	160±20	82 %±5 %	6.19±1.04	52±6[a]
LOPO	78 %±6 %	5.76±0.92[a]	116±20	79 %±6 %[a]	5.82±0.8	43±11[a]
30 % Training	77 %±15 %	6.11±1.36	153±62	79 %±11 %[a]	5.9±0.87[a]	52±16[a]

[a] Better results

The goal of this investigation was to increase the speed of level sets whereas the initial accuracy should not decrease. As for most applications, a real-time response, less than a second, is ideal. Hence, cutting the segmentation time from minutes toward seconds and fractions of a second seems to be the goal of many practice-oriented papers. With respect to accuracy, it is ultimately the user, or a group of users, who will provide a baseline for comparison by creating manual segmentations (ground-truth images). Therefore, the level of agreement between level set results and the ground-truth images, measured via dice coefficient, should be the same with and without the change for speed increase.

Processing time in low resolutions is much shorter than in higher ones. Because the proposed method starts from a resolution lower than the original, the convergence speed was much faster. For each higher resolution, the initial curve is the converged one from the previous (lower) resolution. Thus, it is closer to the prostate boundaries in each higher resolution.

In the first experiment, the overall accuracies obtained using level set method according to Bresson et al. (LS_B) method and the proposed multi-resolution method (LS_B^{MR}) are extremely close. The obvious difference is the convergence speed, where LS_B^{MR} is about 2.5 times faster than LS_B with much more consistency shown by the low standard deviations in Table 2.

The investigated method is semiautomated as the region of interest is expected to be provided by an experienced user. The effect of ROI variations, resulting from variability of human operator's input, was tested as well. Although the performance of the two methods were affected, the multi resolution approach results show that it is less sensitive to larger ROIs. In low resolutions, regions become more homogeneous. The multi-resolution method is benefiting from this because of the region attraction term. Although the ROI size can noticeably affect the outcomes, variability in its location does only minimally change the results.

Shape priors were used to compensate for the weak edges and similar tissue structures surrounding the prostate. The effect of variability of shape priors was studied as well. Shaper priors were constructed using 30 % of the patients, and the remaining 70 % of data were used for testing. Also,

Table 7 Overall summary of results of "premature" multi-resolution level set (LS_B^{MRP}) compared to level set (LS_B) and multi-resolution level set (LS_B^{MR})

Region	Metric			Speed-up		Speed-up
Apex	D	[61 %, 69 %]	[66 %, 70 %]	2.4	[74 %, 77 %][a]	21.3[a]
	d_H	[5.76, 6.28]	[5.75, 6.17]		[5.21, 5.61][a]	
	Time (s)	[129, 170]	[55, 67]		[6, 8][a]	
Midgland	D	[76 %, 79 %]	[77 %, 80 %]	2.6	[78 %, 82 %][a]	17.9[a]
	d_H	[5.50, 5.85]	[5.53, 5.87]		[5.43, 5.76][a]	
	Time (s)	[105, 128]	[43, 49]		[6, 7][a]	
Base	D	[80 %, 83 %][a]	[72 %, 76 %]	2.7	[78 %, 81 %][a]	17.6[a]
	d_H	[4.77, 5.26][a]	[5.10, .64]		[4.79, 5.24][a]	
	Time (s)	[87, 107]	[34, 39]		[5, 6][a]	
Overall	D	[76 %, 79 %]	[77 %, 80 %]	2.6	[78 %, 80 %][a]	17.9[a]
	d_H	[5.50, 5.85]	[5.53, 5.87]		[5.29, 5.62][a]	
	Time (s)	[105, 128]	[43, 49]		[6, 7][a]	

[a] Better results

leave-one-patient-out evaluation was performed on 10 patients. The results of these different evaluations indicate that shape-priors can obviously affect the convergence time, while negligibly affecting the accuracy.

Premature convergence was introduced in an attempt to further accelerate the multi-resolution level set. The idea came from the global-to-local view property of multi-resolution analysis, where the view of an image becomes rather global for coarse resolutions. The local features (i.e., edges) of prostate are minimally contributing to the segmentation process. So, the idea to converge before the original resolution becomes viable because the algorithm will become greatly faster without losing accuracy. The results clearly demonstrated significant acceleration, which could contribute to a real-time segmentation.

Because there is no available automation method for parameter selection yet, they were selected empirically as presented in Table 1. The weights of boundary, region, and shape terms are important, and need to be selected carefully. Because the MRI prostate has weak edges, boundary term should have low weight. Regional information is more important, especially in lower resolutions, thus the region term weight should be selected higher than boundary term. Choosing large value for time step yields faster, but unstable numerical solution of level set function, while choosing small value yields slower computation time. Similarly, selecting high value for number of iterations before re-initialization could cause instability. We believe that setting different parameters for each resolution will enhance the performance of MR-Bresson. For example, as resolution becomes finer, more weight should be set for boundary term and less for region term, and the opposite is true.

Although this study was conducted on 2D images, the findings assumed to be true for 3D images. Because level set algorithm can be easily extended to higher dimensions.

Part of our future work would be automated detection of the ROI and parameter selection. As well, learning to automatically set the optimal resolution level constitutes an urgent problem.

It should be mentioned that we did not observe any topology change between the levels of resolution. However, if this occurs, then the segmentation accuracy might drop. As well, as the prostate gland, in spite of its shape variability, still can be considered as a regular shape, e.g., compared to the malignant tumors or brain regions, one may expect the same level of speed-up but not necessarily the same level of accuracy.

References

1. Osher S, Sethian JA: Fronts propagating with curvature-dependent speed: algorithms based on hamilton-jacobi formulations. J Comput Phys 79(1):12–49, 1988
2. Malladi R, Sethian JA, Vemuri BC: Shape modeling with front propagation: a level set approach. IEEE Trans Pattern Anal Mach Intell 17(2):158–175, 1995
3. R. Toth, P. Tiwari, M. Rosen, A. Kalyanpur, S. Pungavkar, and A. Madabhushi. A multi-modal prostate segmentation scheme by combining spectral clustering and active shape models. In Medical Imaging 2008: Image Processing, volume 6914, page 6914 4S. SPIE, 2008.
4. R. Toth, J. Bulman, A.D. Patel, B. N. Bloch, E. Genega, N. Rofsky, R. Lenkinski, and A Madabhushi. Integrating an adaptive region-based appearance model with a landmark-free statistical shape model: application to prostate MRI segmentation. In SPIE Medical Imaging, volume 7962, page 79622V. SPIE, 2011.
5. A. Tsai, A. Yezzi, W. Wells, C. Tempany, D. Tucker, A. Fan, W.E. Grimson, and A. Willsky. Model-based curve evolution technique for image segmentation. In The IEEE Computer Society Conference on Computer Vision and Pattern Recognition, CVPR, pages I–463 – I–468, 2001.
6. Pasquier D, Lacornerie T, Vermandel M, Rousseau J, Lartigau E, Betrouni N: Automatic segmentation of pelvic structures from magnetic resonance images for prostate cancer radiotherapy. Int J Radiat Oncol Biol Phys 68(2):592–600, 2007
7. Y. Zhang, B. Matuszewski, A. Histace, F. Precioso, J. Kilgallon, and C. Moore. Boundary delineation in prostate imaging using active contour segmentation method with interactively defined object regions. In Prostate Cancer Imaging'10, volume 6367 of Lecture Notes in Computer Science, pages 131–142. Springer Berlin/ Heidelberg, 2010.
8. X. Liu, D.L. Langer, M.A. Haider, T.H. Van der Kwast, A.J. Evans, M.N. Wernick, and I.S. Yetik. Unsupervised segmentation of the prostate using mr images based on level set with a shape prior. In Annual International Conference of the IEEE Engineering in Medicine and Biology Society, EMBC, pages 3613 –3616, 2009.
9. A. Firjani, A. Elnakib, F. Khalifa, A. El-Baz, G. Gimel'farb, M.A. El-Ghar, and A. Elmaghraby. A novel 3d segmentation approach for segmenting the prostate from dynamic contrast enhanced MRI using current appearance and learned shape prior. In IEEE International Symposium on Signal Processing and Information Technology (ISSPIT), pages 137 –143, 2010.
10. A. Firjani, A. Elnakib, F. Khalifa, G. Gimel'farb, M.A. El-Ghar, A. Elmaghraby, and A. El-Baz. A new 3d automatic segmentation framework for accurate extraction of prostate from diffusion imaging. In Biomedical Sciences and Engineering Conference (BSEC), pages 1–4, 2011.
11. N. Makni, P. Puech, R. Lopes, R. Viard, O. Colot, and N. Betrouni. Automatic 3d segmentation of prostate in MRI combining a priori knowledge, markov fields and bayesian framework. In 30th Annual International Conference of the IEEE Engineering in Medicine and Biology Society, EMBS., pages 2992 – 2995, 2008.
12. Martin S, Daanen V, Troccaz J: Atlas-based prostate segmentation using an hybrid registration. Int J Comput Assist Radiol Surg 3:485–492, 2008
13. Martin S, Rodrigues G, Patil N, Bauman G, D'Souza D, Sexton T, Palma D, Louie AV, Khalvati F, Tizhoosh HR, Gaed S: A multiphase validation of atlas-based automatic and semiautomatic segmentation strategies for prostate MRI. Int J Radiat Oncol Biol Phys 85(1):95–100, 2013
14. A. Firjany, A. Elnakib, A. El-Baz, G. L. Gimel'farb, M.A. El-Ghar, and A. Elmagharby. Novel stochastic framework for accurate

segmentation of prostate in dynamic contrast enhanced MRI. In Prostate Cancer Imaging'10, pages 121–130, 2010.

15. D. Flores-Tapia, N. Venugopal, G. Thomas, B. McCurdy, L. Ryner, and S. Pistorius. Real time MRI prostate segmentation based on wavelet multiscale products flow tracking. In Engineering in Medicine and Biology Society (EMBC), 2010 Annual International Conference of the IEEE, pages 5034 –5037, 2010.

16. Daniel Flores-Tapia, Gabriel Thomas, Niranjan Venugopal, Boyd McCurdy, and Stephen Pistorius. Semi automatic MRI prostate segmentation based on wavelet multiscale products. In 30th Annual International Conference of the IEEE Engineering in Medicine and Biology Society, EMBS, pages 3020 –3023, 2008.

17. M. Samiee, G. Thomas, and R. Fazel-Rezai. Semi-automatic prostate segmentation of mr images based on flow orientation. In IEEE International Symposium on Signal Processing and Information Technology, pages 203 –207, 2006.

18. R. Zwiggelaar, Y. Zhu, and S. Williams. Semi-automatic segmentation of the prostate. In Pattern Recognition and Image Analysis, volume 2652 of Lecture Notes in Computer Science, pages 1108–1116. Springer Berlin/ Heidelberg, 2003.

19. F. Sahba, H.R. Tizhoosh, M.M. Salama, A coarse-to-fine approach to prostate boundary segmentation in ultrasound images, Biomedical engineering online 4 (1), 58, 2005.

20. F. Sahba, H.R. Tizhoosh, M.M. Salama, Segmentation of prostate boundaries using regional contrast enhancement, Image Processing, 2005. ICIP 2005. IEEE International Conference on 2, II-1266-9, 2005.

21. H.R. Tizhoosh, G. Krell, B. Michaelis, Locally adaptive fuzzy image enhancement, Computational Intelligence Theory and Applications, 272–276, 1997.

22. S. Rahnamayan, H.R. Tizhoosh, M.M. Salama, Automated snake initialization for the segmentation of the prostate in ultrasound images, Image Analysis and Recognition, 930–937, 2005.

23. Bustince H, Pagola M, Barrenechea E, Fernández J, Melo-Pinto P, Couto P, Tizhoosh HR, Montero J: Ignorance functions. An application to the calculation of the threshold in prostate ultrasound images. Fuzzy Sets Syst 161(1):20–36, 2010

24. Losasso F, Talton JO, Kwatra N, Fedkiw R: Two-way coupled SPH and particle level set fluid simulation. IEEE Trans Vis Comput Graph 14(4):797–804, 2008

25. Brodersen A, Museth K, Porumbescu S, Budge B: Geometric texturing using level sets. IEEE Trans Vis Comput Graph 14(2):277–288, 2008

26. Kim YS, Byun JK, Park IH: A level set method for shape optimization of electromagnetic systems. IEEE Trans Magn 45(3):1466–1469, 2009

27. A. Ghodrati, F. Calderero, D.H. Brooks, G. Tadmor, and R. MacLeod. A level sets algorithm for the inverse problem of electrocardiography. In Thirty-Eighth Asilomar Conference on Signals, Systems and Computers, volume 2, pages 1590 – 1594, 2004.

28. Caselles V, Catté F, Coll T, Dibos F: A geometric model for active contours in image processing. Numer Math 66:1–31, 1993

29. Malladi R, Sethian J, Vemuri B: Evolutionary fronts for topology-independent shape modelling and recovery, volume 800 of Lecture Notes in Computer Science. Springer, Berlin/ Heidelberg, 1994, pp 1–13

30. V. Caselles, R. Kimmel, and G. Sapiro. Geodesic active contours. In Fifth International Conference on Computer Vision, pages 694 –699, 1995.

31. Caselles V, Kimmel R, Sapiro G: Geodesic active contours. Int J Comput Vis 22(1):61–79, 1997

32. S. Kichenassamy, A. Kumar, P. Olver, A. Tannenbaum, and A. Yezzi. Gradient flows and geometric active contour models. In Fifth International Conference on Computer Vision, pages 810 –815, 1995.

33. Yezzi Jr, A, Kichenassamy S, Kumar A, Olver P, Tannenbaum A: A geometric snake model for segmentation of medical imagery. IEEE Trans Med Imaging 16(2):199–209, 1997

34. K. Siddiqi, Y.B. Lauziere, A. Tannenbaum, and S.W. Zucker. Area and length minimizing flows for shape segmentation. In IEEE Computer Society Conference on Computer Vision and Pattern Recognition, pages 621 –627, 1997.

35. Mumford D, Shah J: Optimal approximations by piecewise smooth functions and associated variational problems. Commun Pure Appl Math 42(5):577–685, 1989

36. Chan TF, Vese LA: Active contours without edges. IEEE Trans Image Process 10(2):266–277, 2001

37. Vese LA, Chan TF: A multiphase level set framework for image segmentation using the Mumford and Shah model. Int J Comput Vis 50(3):271–293, 2002

38. Jr. Yezzi, A., A. Tsai, and A. Willsky. A statistical approach to snakes for bimodal and trimodal imagery. In The Proceedings of the Seventh IEEE International Conference on Computer Vision, volume 2, pages 898 –903 vol.2, 1999.

39. Tsai Jr, A, Yezzi A, Willsky AS: Curve evolution implementation of the Mumford-Shah functional for image segmentation, denoising, interpolation, and magnification. IEEE Trans Image Process 10(8): 1169–1186, 2001

40. Y.Chen, S. Thiruvenkadam, H.D. Tagare, F. Huang, D. Wilson, and E.A. Geiser. On the incorporation of shape priors into geometric active contours. In IEEE Workshop on Variational and Level Set Methods in Computer Vision, pages 145 – 152, 2001.

41. M.E. Leventon, W.E.L. Grimson, and O. Faugeras. Statistical shape influence in geodesic active contours. In 5th IEEE EMBS International Summer School on Biomedical Imaging, 2002.

42. T. Riklin-Raviv, N. Kiryati, and N. Sochen. Prior-based segmentation by projective registration and level sets. In Tenth IEEE International Conference on Computer Vision, ICCV, pages 204 – 211 Vol. 1, 2005.

43. T. Riklin-Raviv, N. Kiryati, and N. Sochen. Segmentation by level sets and symmetry. In IEEE Computer Society Conference on Computer Vision and Pattern Recognition, pages 1015 – 1022, 2006.

44. Bresson X, Vandergheynst P, Thiran JP: A variational model for object segmentation using boundary information and shape prior driven by the Mumford-Shah functional. Int J Comput Vis 68:145–162, 2006

45. P.-Y. Tsang. Multi-resolution image segmentation using geometric active contours. Master's thesis, University of Waterloo, Waterloo, Ontario, Canada, 2004.

46. N. Lin, W. Yu, and J. S. Duncan. Combinative multi-scale level set framework for echocardiographic image segmentation. In Proceedings of the 5th International Conference on Medical Image Computing and Computer-Assisted Intervention-Part I, MICCAI'02, pages 682–689, 2002.

47. Lin N, Yu W, Duncan JS: Combinative multi-scale level set framework for echocardiographic image segmentation. Med Image Anal 7(4):529–537, 2003

48. A.P. Witkin. Scale-Space Filtering. In 8th Int. Joint Conf. Artificial Intelligence, volume 2, pages 1019–1022, 1983.

49. Bresson X, Vandergheynst P, Thiran JP: Multiscale active contours. Int J Comput Vis 70:197–211, 2006

50. Ma J, Shan H: Curvelet-based geodesic snakes for image segmentation with multiple objects. Pattern Recogn Lett 31(5):355–360, 2010

51. F.S. Al-Qunaieer, H.R. Tizhoosh, and S. Rahnamayan. Multi-resolution level set image segmentation using wavelets. In 18th IEEE International Conference on Image Processing (ICIP), pages 269 –272, 2011.

52. Chen Y, Tagare HD, Thiruvenkadam S, Huang F, Wilson D, Gopinath KS, Briggs RW, Geiser EA: Using prior shapes in geometric active contours in a variational framework. Int J Comput Vis 50: 315–328, 2002

53. Burt P, Adelson E: The Laplacian pyramid as a compact image code. IEEE Trans Commun 31(4):532–540, 1983

54. Dabov K, Foi A, Katkovnik V, Egiazarian K: Image denoising by sparse 3-d transform-domain collaborative filtering. IEEE Trans Image Process 16(8):2080–2095, 2007

55. Zuiderveld K: Contrast limited adaptive histogram equalization. Academic Press Professional, Inc., San Diego, CA, USA, 1994, pp 474–485

56. Prostate MR Image Database. Prostate MR Image Database. http://prostateMRimageDatabase.com.

57. Dice LR: Measures of the amount of ecologic association between species. Ecology 26(3):297–302, 1945

58. Huttenlocher DP, Klanderman GA, Rucklidge WJ: Comparing images using the Hausdorff distance. IEEE Trans Pattern Anal Mach Intell 15(9):850–863, 1993